Available online at www.sciencedirect.com
SCIENCE DIRECT®
Polymer 44 (2003) 6089–6101
polymer
www.elsevier.com/locate/polymer

Micromechanical modeling of intraspherulitic deformation of semicrystalline polymers

J.A.W. van Dommelen[a,*], D.M. Parks[b], M.C. Boyce[b], W.A.M. Brekelmans[a], F.P.T. Baaijens[a]

[a]*Dutch Polymer Institute, Department of Mechanical Engineering, Eindhoven University of Technology, P.O. Box 513, 5600 MB, Eindhoven, The Netherlands*
[b]*Department of Mechanical Engineering, Center for Materials Science and Engineering, Massachusetts Institute of Technology, Cambridge, MA 02139, USA*

Received 20 March 2003; received in revised form 30 May 2003; accepted 2 June 2003

Dedicated to Prof. Ian M. Ward on the occasion of his 75th birthday

Abstract

Semicrystalline polymers often show a spherulitic morphology, consisting of a radial assembly of twisted crystalline lamellae and amorphous layers. A multiscale numerical model is used to investigate the mechanics of intraspherulitic deformation of polyethylene. The model establishes links across the microscopic, the mesoscopic, and the macroscopic levels. Constitutive properties of the material are identified for the crystallographic and amorphous domains. The averaged fields of an aggregate of individual phases, having preferential orientations, form the constitutive behavior of intraspherulitic material. The spherulitic macrostructure is described by finite element models. The macroscopic stress–strain response resembles that of a previous random polycrystalline model. However, the current model includes the geometrical effect of the anisotropic structure within a spherulite, causing strain concentrations in the centers, which spread out in the equatorial region for uniaxial loading conditions and in inclined directions for plane strain loading. The deformations are linked to microstructural processes as interlamellar deformation and intralamellar crystallographic slip.

Keywords: Micromechanics; Semicrystalline; Spherulite

1. Introduction

The mechanical performance of semicrystalline polymeric materials, as characterized by elasto-viscoplastic deformation, is strongly dependent on the underlying microstructure [1–3]. Much research has been focused on understanding the viscoplastic behavior of semicrystalline polymers with experimental and modeling studies [4–22], relating the macroscopic behavior to the morphology.

When cooled from the melt, many polymers, such as for example polyethylene, possess a semicrystalline structure often with a spherulitic morphology [3,23–25]. Considered from a central point, each spherulite consists of a radial assembly of thin crystalline lamellae which are separated by amorphous layers. Any macroscopically homogeneous deformation of these materials is accommodated by various deformation mechanisms in the heterogeneous microstructure. For a better understanding of the mechanical behavior of semicrystalline materials, a link between the macroscopic and microscopic levels should be established. Early investigations considered modeling the polymer as an aggregate of anisotropic elastic microstructural units [1, 26–31]. The often applied classical Voigt and Reuss averaging schemes provide upper and lower bounds, respectively, for the macroscopic behavior. A rigid/viscoplastic two-phase aggregate model was developed by Lee et al. [12,13], introducing a class of hybrid interaction models, which constitute an intermediate approach between the upper and lower bounds. An elasto-viscoplastic model for the behavior of semicrystalline materials was presented by Van Dommelen et al. [32]. However, in these aggregate models, the effects of the spherulitic geometry are absent.

A review of the structure and microscopic deformation mechanisms of polyethylene spherulites is given by Lin and Argon [2]. Experimental investigations of intraspherulitic deformation processes have been carried out for thin films. Both affine and nonaffine deformation models of spherulites were proposed by Wilchinsky [33]. Hay and Keller [34] found spherulitic deformation to consist mostly of a combination of homogeneous and inhomogeneous deformation. The latter was found to occur predominantly within

* Corresponding author. Tel.: +31-40-2475701; fax: +31-40-2447355.
E-mail address: j.a.w.v.dommelen@tue.nl (J.A.W. Van Dommelen).

0032-3861/03/$ - see front matter © 2003 Elsevier Ltd. All rights reserved.
doi:10.1016/S0032-3861(03)00558-5

spherulites in the equatorial region (the *equator* denotes the region where the radial direction is perpendicular to the tensile loading direction) by (100)[001] slip, causing a rotation of crystals around the *b*-axis for appropriately oriented crystals, and between spherulites in the polar regions (the *pole*is defined as the region of the spherulite where the radial direction is aligned with the loading axis) of the boundary. Deformations in the equatorial area were observed to be higher than in the polar area, with the strain becoming very large towards the center of the spherulite. Neck formation across the transverse diameter in spherulitic films of polyethylene was reported by Keith and Padden [35]. Kobayashi and Nagasawa [36] used a rigid/plastic Hill yield criterion to model the heterogeneous distribution of deformation in a spherulite. Wang [37] attributed the inhomogeneous deformation primarily to the anisotropic structure of the spherulite, and secondarily to the mechanical interactions between spherulites. Based on a linearly elastic model of a spherulite, Wang [37] found the stress and strain to go to infinity in the spherulitic center, and the strain in the equatorial region to be larger than in the polar region. In the inclined 45° area, the deformation was concluded to be dominated by shear strain. Allan and Bevis [38,39] reported the occurrence of twinning in the equatorial regions of thin films of polyethylene spherulites. They subdivided the spherulitic domain into three regions: (i) the equatorial region, (ii) the region where the angle between the radial direction and the tensile axis ranges from 30 to 55°, here referred to as the *inclined* region, and (iii) the polar area. The *b*-axis governs the deformation behavior in all three regions, with a tendency to align the *c*-direction towards the tensile axis. The polar region was concluded to possess a larger deformation resistance with respect to the loading direction than the other regions. The primary mode of deformation is interlamellar slip, followed by intralamellar slip. The interspherulitic boundaries were reported to be the weakest regions in polyethylene thin films by Butler and Donald [40]. Aboulfaraj et al. [41] found the deformation to be initiated near the center of polypropylene spherulites, and observed little deformation in the polar region, and largest strains in the equatorial area. The inclined area was concluded to be the region of the spherulite with the highest compliance by Brooks et al. [42]. A spherulitic model, based on rigid crystalline lamellae and a molecular theory for the amorphous domains, subjected to affine deformation, was developed by Nitta [43]. A finite element model of alternating amorphous and crystalline layers was presented by Doyle [44] for polyethylene, and was found to provide a quantitatively good prediction of the dependence of the elastic modulus on the crystallinity for relatively high crystallinities.

In this work, a multiscale numerical model is used to investigate the mechanics of intraspherulitic deformation for polyethylene, taking into account the geometry of the spherulites. For this purpose, a distinction between three different scales is made, as is schematically shown in Fig. 1.

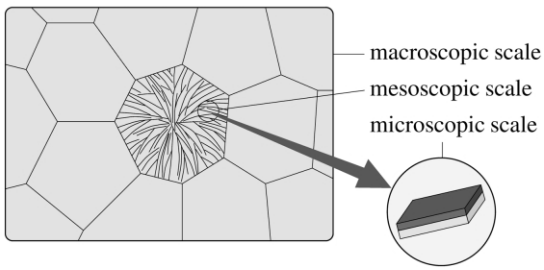

Fig. 1. Schematic illustration of a polyspherulitic structure, with one spherulite highlighted and an indication of the various modeling levels.

Macroscopically, a structure of multiple spherulites is considered, which will be modeled by finite elements. Different representative volume element (RVE) models are used for either uniaxial or plane strain deformation. In each material point within a spherulite, referred to as the mesoscopic level, an assembly of twisted, and locally parallel lamellae is assumed. The mechanical behavior of this assembly is modeled by a polycrystalline composite inclusion model [32]. The basic element of this model is a two-phase layered structure of a crystalline and an amorphous domain. Constitutive properties are assigned to the components at this microscopic level. The microstructural behavior is linked to the mesoscopic and the macroscopic scales. The calculations provide a further insight in the mechanics of deformation of semicrystalline polymers.

2. Microscopic scale: material models

The anisotropic constitutive behavior of intraspherulitic material is modeled by an aggregate of elasto-viscoplastic two-phase composite inclusions [12,13]. Each inclusion consists of a crystalline and an amorphous phase. In this section, the constitutive models of the constituent phases are shortly discussed. For a more elaborate presentation of these models, see Van Dommelen et al. [32].

2.1. Crystalline phase

The crystalline domain of polymeric material consists of regularly ordered molecular chains. The crystal structure results in (i) anisotropic elastic behavior where the elastic properties are given with respect to the crystallographic directions, and (ii) plastic deformation governed primarily by crystallographic slip on a limited number of slip planes [3,18]. Moreover, plastic deformation may result from mechanical twinning or stress-induced martensitic phase transformations [2,3,45,46]. Since crystallographic slip is assumed to be of most importance, in the modeling process the latter two mechanisms are left out of consideration.

The elastic component of the deformation in the crystalline phase is characterized by an anisotropic fourth-order elastic modulus tensor. The anisotropic elastic

properties are coupled to the crystallographic directions. For the viscoplastic behavior of the crystalline phase, a rate-dependent crystal plasticity model is used. In this model, the plastic velocity gradient of the crystalline lamella, consisting of a single crystal, is composed of the contributions of all physically distinct slip systems, being 8 for high density polyethylene (HDPE), with a lowest slip resistance of 8 MPa. The shear rate of each slip system is assumed to be related to the resolved shear stress according to a viscoplastic power law.

2.2. Amorphous phase

The amorphous phase of semicrystalline polymeric material consists of an assembly of disordered macromolecules, which are morphologically constrained by the neighboring crystalline lamellae. Plastic deformation in these domains occurs by the thermally activated rotation of segments. At room temperature, the amorphous phase of HDPE, which is the material of interest in this work, is in the rubbery regime, with the glass transition temperature near −70 °C. However, the amorphous phase of other semicrystalline polymers, e.g. nylon, with a higher glass transition temperature, need to be modeled as elasto-viscoplastic.[1]

The initial elastic resistance of the rubbery amorphous phase is well below the elastic resistance of the crystalline domain. Consequently, elastic deformations can be considerably large and are modeled by a generalized neo-Hookean relationship. A relatively strain rate-insensitive viscoplastic power law relation between an effective shear strain rate and the effective shear stress [12] is used in conjunction with a back stress tensor for which the Arruda–Boyce eight-chain network model of rubber elasticity [47] is used.

3. Mesoscopic scale: composite inclusion model

The mechanical behavior at the mesoscopic level is modeled by an aggregate of layered two-phase composite inclusions as was first proposed by Lee et al. [12,13] for rigid/viscoplastic material behavior. Each separate composite consists of a crystalline lamella which is mechanically coupled to its corresponding amorphous layer, as is shown in Fig. 2.

The stress and deformation fields within each phase are assumed to be piecewise homogeneous; however, they may differ between the two coupled phases. It is assumed that the crystalline and amorphous components remain fully mechanically coupled. Interface compatibility within the composite inclusion and traction equilibrium across the interface are enforced. To relate the volume-averaged

[1] For the purpose of generality, an elasto-viscoplastic approach is used in the composite inclusion model [32].

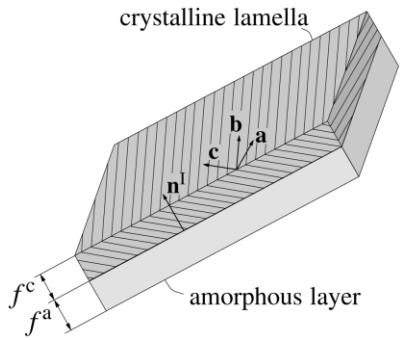

Fig. 2. Schematic illustration of a layered two-phase composite inclusion.

mechanical behavior of each composite inclusion to the imposed boundary conditions for an aggregate of inclusions, a hybrid local–global interaction law is used. This class of hybrid-inclusion models was introduced by Lee et al. [12,13] for rigid/viscoplastic composite inclusions. A more detailed description of the composite inclusion model is presented elsewhere [32]. Some aspects of the finite element implementation in ABAQUS [48] are given in Van Dommelen et al. [49].

In Section 4, the anisotropy of preferentially oriented intraspherulitic material, as predicted by the composite inclusion model, will be investigated. A mesoscopic aggregate of composite inclusions, represented by a set of crystallographic orientations and corresponding lamellar orientations, will be subjected to constant strain rate uniaxial tension in the three principal directions $\mathbf{e}_i$ of the material coordinate system. Consider the right polar decomposition $\bar{\mathbf{F}} = \bar{\mathbf{R}}\cdot\bar{\mathbf{U}}$ of the volume-averaged deformation gradient, where $\bar{\mathbf{R}}$ is the mesoscopic rotation tensor, and $\bar{\mathbf{U}}$ is the corresponding right stretch tensor. Then, the following conditions are imposed:

$$\bar{\mathbf{R}} = \mathbf{I}; \qquad \bar{U}_{ii} = \lambda(t); \qquad i = 1 \vee i = 2 \vee i = 3, \tag{1}$$

with

$$\lambda(t) = \exp(\dot{\varepsilon}t), \tag{2}$$

where $\dot{\varepsilon}$ is set equal to the material reference shear rate $\dot{\gamma}_0$. Furthermore, the components of the Cauchy stress tensor should satisfy:

$$\bar{\sigma}_{jj} = \bar{\sigma}_{12} = \bar{\sigma}_{13} = \bar{\sigma}_{23} = 0; \qquad j \in \{1,2,3 | j \neq i\}. \tag{3}$$

In another test case, pure shear deformation is applied by prescribing one of the basic shear components ij of the (symmetric) right stretch tensor

$$\bar{\mathbf{R}} = \mathbf{I}; \qquad \bar{U}_{ij} = \gamma(t); \qquad ij = 12 \vee ij = 13 \vee ij = 23, \tag{4}$$

with

$$\gamma(t) = \tfrac{1}{2}\sqrt{3}\dot{\gamma}_0 t, \tag{5}$$

and

$$\bar{\sigma}_{11} = \bar{\sigma}_{22} = \bar{\sigma}_{33} = \bar{\sigma}_{kl} = 0; \qquad kl \in \{12, 13, 23 | kl \neq ij\}. \tag{6}$$

4. Intraspherulitic material

A schematic illustration of a spherulitic structure is shown in Fig. 3(a). Crystalline lamellae, interspersed with amorphous regions, grow in an approximately radial direction from a central nucleus [2,3,38].

This rather complicated structure will be approximated by assuming that all lamellae have grown in a perfectly radial direction with respect to the center, represented by a local coordinate system with its 1-axis in the radial direction, as is shown in Fig. 3(b). For polyethylene spherulites, having an orthorhombic lattice, this growth direction corresponds with the crystallographic (010)-direction, with a twist around this b-axis, as schematically depicted in Fig. 4(a).

Consequently, the principal crystallographic a and c-axes, the latter corresponding to the molecular chain direction, exhibit a rotation around the b-axis, with increasing radial distance, as shown in Fig. 4(b). As a representative mesoscopical unit for the intraspherulitic material of meltcrystallized HDPE, a bundle of radiating lamellae with multiple twisting periods is assumed. Therefore, the mesoscopic constitutive behavior will show a fiber symmetry around the local 1-direction. This material is modeled by an aggregate of composite inclusions with preferential initial orientations of the crystallographic domains, where the (010) poles are, except for an additional randomness, parallel to the 1-direction. The distribution of orientations of the principal lattice directions is represented in Fig. 5(a)–(c) for 125 composite inclusions, representing the intraspherulitic domain.

Experimental studies of meltcrystallized polyethylene show that lamellar surfaces are of the $\{h0l\}$-type, where the angle between the chain direction c and the lamellar normal $\mathbf{n}^{\mathrm{I}}$ varies between 20 and 40° [23,50]. Gautam et al. [51] have found, by molecular simulations, the $\{201\}$ planes, having a chain tilt angle of 35°, to provide the lowest crystal/amorphous interface energy. Here, the initial angle between $\mathbf{c}_0$ and $\mathbf{n}^{\mathrm{I}}_0$ is set at 35°, corresponding to the $\{201\}$ planes. Consequently, the lamellar normals are approximately perpendicular to the spherulitic radial direction. The initial orientations of the lamellar normals are shown in Fig. 5(d). The material properties at the microscopic level, are adopted from Ref. [32].

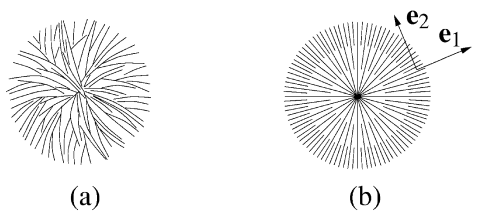

Fig. 3. (a) Structure of a spherulite (after Ref. [3]), and (b) simplified model.

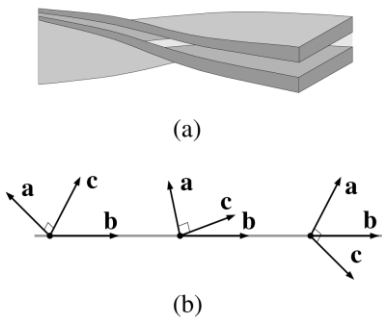

Fig. 4. (a) Twisting of a lamella (after Ref. [38]), and (b) orientation of the crystallographic directions in a lamella.

The mesoscopic aggregate is loaded in the different modes, as previously described (i.e. uniaxial tension and pure shear). The obtained equivalent mesoscopic stress $\bar{\sigma}^{\mathrm{eq}} = \sqrt{\frac{3}{2}\bar{\boldsymbol{\sigma}}^{\mathrm{d}} : \bar{\boldsymbol{\sigma}}^{\mathrm{d}}}$, with $\bar{\boldsymbol{\sigma}}^{\mathrm{d}} = \bar{\boldsymbol{\sigma}} + \bar{p}\mathbf{I}$ the mesoscopic deviatoric stress tensor and $\bar{p} = -\frac{1}{3}\mathrm{tr}(\bar{\boldsymbol{\sigma}})$ the mesoscopic hydrostatic pressure, as a function of the imposed deformation, is represented in Fig. 5(e). The results are normalized by the lowest slip resistance $\tau_0 = 8$ MPa. The constitutive behavior at the mesoscopic scale (i.e. of the intraspherulitic domains) should be transversely isotropic with the fiber symmetry direction corresponding to the spherulitic radial direction. Therefore, all differences in mechanical response in the 22 and 33 tensile directions and the 12 and 13 shear directions are of statistical origin. The viscoplastic part of the crystalline constitutive model provides eight distinct slip systems for polyethylene [52]. However, when loaded in the b-direction, only the $\{110\}\langle 1\bar{1}0\rangle$ slip systems can accommodate plastic crystalline deformation, whereas the (100) slip planes, having the lowest slip resistance, are not activated. As a consequence, a relatively elevated yield stress in the 1-direction is observed. In the plastic range, the ratio of $\bar{\sigma}_{11}/\bar{\sigma}_{22}$ is approximately 1.4. The direction with the elevated yield resistance will be oriented in the tensile direction in the polar areas of a spherulite under uniaxial tension, and perpendicular to the tensile direction in the equatorial region.

The number of inclusions within an aggregate should be sufficiently large, in order to expel the influence of the particular set of initial inclusions, and to mimic a transversely isotropic mesoscopic material behavior. Here, the number of inclusions that comprise an aggregate is limited to 125, hence a quasi transversely isotropic response is obtained. The influence of the aggregate size on the mesoscopic behavior was demonstrated in Van Dommelen et al. [49].

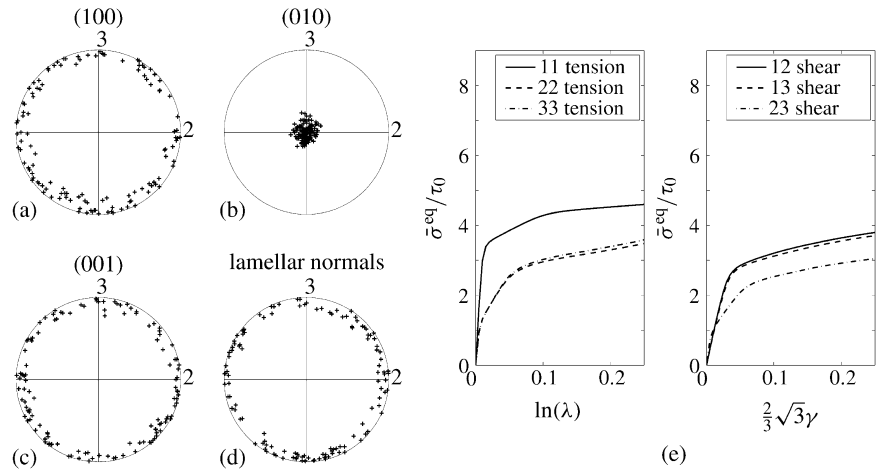

Fig. 5. Equal area projection pole figures with (a)–(c) the principal crystallographic lattice directions, and (d) the lamellar normals of a set of orientations representing intraspherulitic material and (e) the normalized equivalent mesoscopic stress $\bar{\sigma}^{eq}/\tau_0$, vs. the imposed deformation for tension and shear in the mesoscopic material principal directions as predicted by the composite inclusion model.

5. Macroscopic scale: spherulitic models

A macroscopic structure with multiple spherulites is modeled by finite elements. Different RVE models are used for either uniaxial or plane strain deformation. For the latter, also the irregularity of the structure is accounted for.

5.1. Axisymmetric RVE

An axisymmetric RVE model of a staggered array (referred to as the *SA model*) of spherulites is considered, which was previously used for the study of the micromechanics of particle-toughened polymers by Socrate and Boyce [53] and by Tzika et al. [54] and which corresponds to a body centered tetragonal stacking. A schematic representation of the RVE, with $L_0 = R_0$, is shown in Fig. 6(a).

A spherulitic center is assumed to be located in point C_1. Fig. 6(b) shows the location of neighboring RVEs and the corresponding arrangement of spherulites. The spherulites are assumed to be the result of a uniform radial crystal growth; i.e. the spherulitic boundaries are located such that the distances to the nearest centers are equal. The staggered arrangement of spherulites is realized by subjecting the RVE to anti-symmetry conditions (with respect to point M) along the outer radius [55,56]. Axial compatibility along the radial boundary Γ_{34} is written in terms of the axial displacement u_z :

$$u_z(z_0|_M - \eta) + u_z(z_0|_M + \eta) = 2u_z|_M. \tag{7}$$

The combined cross-sectional area of neighboring cells is assumed to remain constant along the axial coordinate; the radial displacement u_r therefore satisfies:

$$[R_0 + u_r(z_0|_M - \eta)]^2 + [R_0 + u_r(z_0|_M + \eta)]^2 = 2[R_0 + u_r|_M]^2. \tag{8}$$

Symmetry conditions along the right and left boundaries are written as

$$u_z|_{\Gamma_{23}} = u_z|_{C_2}; \tag{9}$$

$$u_z|_{\Gamma_{14}} = u_z|_{C_1}, \tag{10}$$

respectively. Since the axis of rotational symmetry coincides with boundary Γ_{12}, the following condition is imposed on this boundary:

$$u_r|_{\Gamma_{12}} = 0. \tag{11}$$

The axisymmetric RVE is subjected to tension at a macroscopically constant strain rate

$$u_z|_{C_2} - u_z|_{C_1} = L_0[\exp(\dot{\varepsilon}t) - 1], \tag{12}$$

where the deformation rate ε is set equal to the material reference shear rate $\dot{\gamma}_0$.

The finite element mesh of the axisymmetric SA model is visualized in Fig. 6(c). Further on, microscopic responses will be shown for the elements that are marked A and B. In each integration point of the 256 reduced integration four-noded bilinear elements, a local coordinate system $\mathbf{e}_i$ is generated. The local 1-directions are shown in Fig. 6(d). In the local coordinate system of each integration point, a unique set of initial crystallographic and lamellar orientations was generated, similar to the distribution that was shown in Fig. 5(a)–(d), where the local 1-directions correspond to the view direction of the pole figures. Finally, in Section 6.2, this RVE will also be employed, using plane strain conditions.

In this work, the periodic twisting in the radial direction is modeled by employing in each integration point an

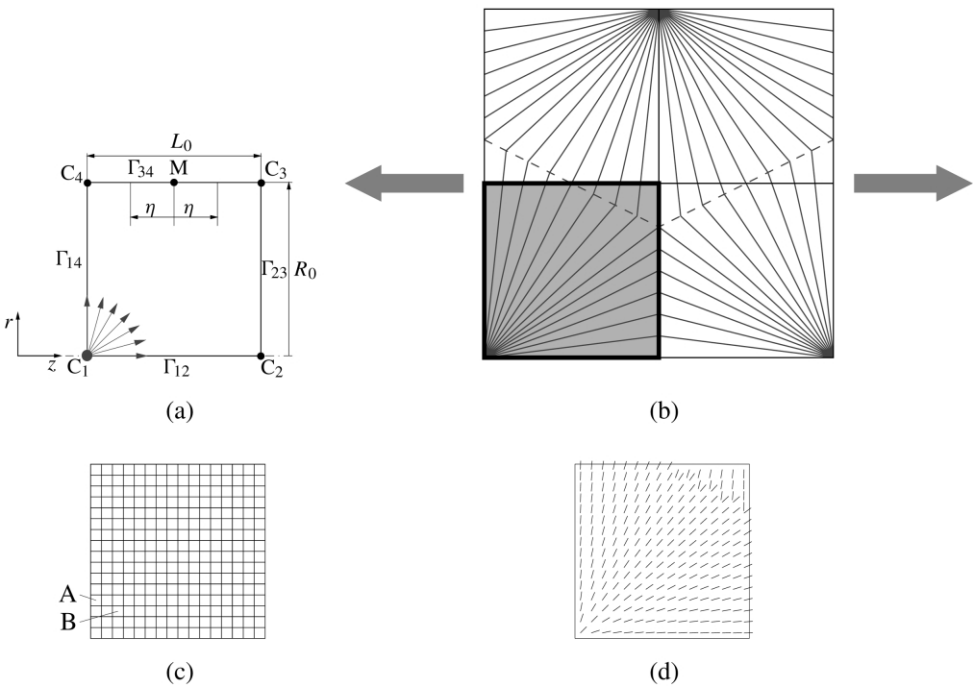

Fig. 6. (a) Schematic visualization of the axisymmetric RVE model of a staggered array of spherulites, (b) the RVE with three neighboring RVEs, (c) finite element mesh and (d) local material orientations.

aggregate of composite inclusions with a fiber symmetry around the local *b*-axes, which are oriented parallel to each other. A twisting period of about 2 μm was reported by Keller and Sawada [50] for polyethylene. With the size of spherulites typically being 50–100 μm, the element size is of the order of one twisting period. A more refined model would be obtained if the length scale of an aggregate would be assumed to be considerably smaller than the wavelength of twisting, i.e. if the twisting nature would be macroscopically modeled rather than mesoscopically. However, this approach would require considerably more refined finite element meshes.

5.2. Irregular plane strain RVE

To account for the irregular nature of spherulitic semicrystalline material, also a plane strain RVE with irregularly dispersed spherulites (referred to as the *ID model*) is used, see Fig. 7(a). The plane strain assumption implies that all deformations in the out-of-plane direction are constrained. Furthermore, a tensile deformation is prescribed in the *x*-direction, whereas the deformations in *y*-direction are unprescribed.

Full compatibility of each opposite boundary pair is assumed. The corresponding kinematic and natural boundary tyings [57] for related points on opposite boundaries are given by

$$\mathbf{u}|_{\Gamma_{34}} - \mathbf{u}|_{C_4} = \mathbf{u}|_{\Gamma_{12}} - \mathbf{u}|_{C_1}; \tag{13}$$

$$\mathbf{u}|_{\Gamma_{14}} - \mathbf{u}|_{C_1} = \mathbf{u}|_{\Gamma_{23}} - \mathbf{u}|_{C_2}; \tag{14}$$

$$\boldsymbol{\sigma}\cdot\mathbf{n}|_{\Gamma_{12}} = -\boldsymbol{\sigma}\cdot\mathbf{n}|_{\Gamma_{34}}; \tag{15}$$

$$\boldsymbol{\sigma}\cdot\mathbf{n}|_{\Gamma_{14}} = -\boldsymbol{\sigma}\cdot\mathbf{n}|_{\Gamma_{23}}, \tag{16}$$

where $\mathbf{n}$ denotes the outward unit normal of the boundary. A tensile loading condition is prescribed on vertex C_2, and is given by

$$u_x|_{C_2} - u_x|_{C_1} = L_0[\exp(\dot{\varepsilon}t) - 1], \tag{17}$$

where $\dot{\varepsilon}$ is set equal to the reference strain rate $\dot{\gamma}_0$ of the material. Furthermore, rotations are prevented by the following condition for the vertices C_1 and C_2 :

$$u_y|_{C_1} = u_y|_{C_2}. \tag{18}$$

The displacements of C_4 are unspecified and follow from equilibrium, whereas the displacements of C_3 are tied to the other vertices. A structure with six irregularly dispersed spherulitic nuclei is taken. The mesh with 576 four-noded bilinear reduced integration plane strain elements is shown in Fig. 7(b).

The formation of a spherulitic grain structure of polypropylene was characterized by Kamal et al. [58], and consists of simultaneous nucleation, followed by uniform growth of the spherulites with the same constant front velocity, which ends by the impingement of spherulites, forming straight boundaries. A local orientation field is generated according to this mechanism. The local 1-direction are taken in the direction of the closest nucleus, taking into account the periodicity of the structure, and is shown in Fig. 7(c). Spherulitic boundaries are located at an

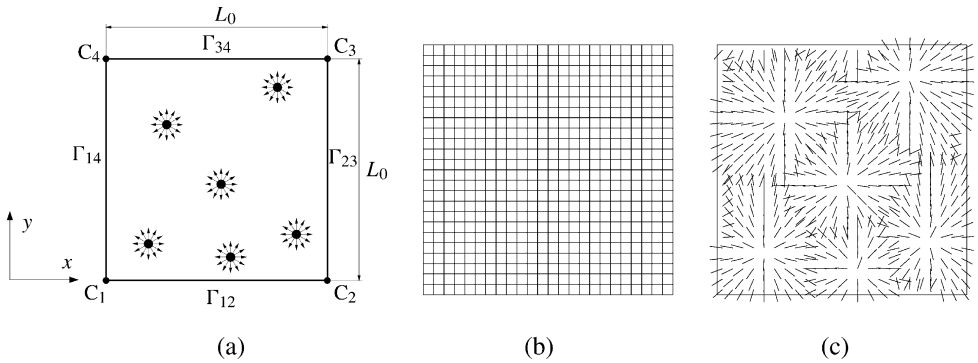

Fig. 7. (a) Schematic visualization of the plane strain RVE with an irregular distribution of spherulite centers, (b) finite element mesh and (c) local material orientations.

equal distance to the two closest nuclei, and are present by the virtue of a discontinuous transition in local material orientations.

6. Results

In this section, the multiscale model will be used to investigate intraspherulitic deformation and stress. Both RVE models, as described in the previous section, are used. In each integration point a (unique) set of orientations with a similar distribution as in Fig. 5(a)–(d), representing a bundle of twisted lamellae, is assumed. The local (fiber) symmetry directions correspond to the 1-directions as described in Section 5. In each integration point, 64 composite inclusions per aggregate are used.

6.1. Axisymmetry

The axisymmetric SA model represents a polyethylene spherulite, with an initial crystallinity of $f^c = 0.7$, under uniaxial loading conditions. In Fig. 8, the obtained fields of the magnitude of plastic deformation, $\bar{\varepsilon}_p^{mag} = \sqrt{\frac{2}{3}\bar{\boldsymbol{\varepsilon}}_p : \bar{\boldsymbol{\varepsilon}}_p}$, with $\bar{\boldsymbol{\varepsilon}}_p$ a mesoscopic plastic strain tensor quantity, are shown for different levels of macroscopically imposed deformation $\dot{\varepsilon}t$. In this figure, z is the loading direction.

The heterogeneous response results from microstructural orientation effects. Plastic deformation is found to be initiated in the center of the spherulite, and spreads out initially in the equatorial direction. At somewhat larger strains, the deformation remains predominantly concentrated in the center, and spreads out with an angle in the range of 0–35° with the equator, forming a lobe at 35°. Moreover, a small concentration of deformation is found at the spherulite boundary.

Some selected microscopic texture evolutions and deformation quantities are shown in Figs. 9 and 10, respectively, for the SA model.

In the pole figures showing the evolution of crystallographic and morphological texture (Fig. 9), each initial orientation is represented by a dot. The arrow connects it with the corresponding final orientation, which is located at the arrow-head. In the pole figures showing microscopic deformation quantities (Fig. 10), the location of each dot represents the initial orientation of the lamellar normal of an inclusion and its gray intensity represents the value of the indicated quantity for the inclusion. The latter pole figures are enriched by reflecting each pole with respect to the central point of the plot. The view direction is the macroscopic out-of plane direction. *Intralamellar* deformation of the ith inclusion is represented by the magnitude of deformation of the crystalline phase, $(\boldsymbol{\varepsilon}^{c^i})^{mag} = \sqrt{\frac{2}{3}\boldsymbol{\varepsilon}^{c^i} : \boldsymbol{\varepsilon}^{c^i}}$, with $\boldsymbol{\varepsilon}$ the logarithmic strain tensor. For the amorphous deformation, a distinction is made between *interlamellar shear* and *interlamellar separation*. Let $\mathbf{y}^{a^i}$ be a material vector in the amorphous phase of inclusion i, with $\mathbf{y}_0^{a^i} = \mathbf{n}_0^{I^i}$. Then, interlamellar shear is assumed to be represented by the angle (in radians) between

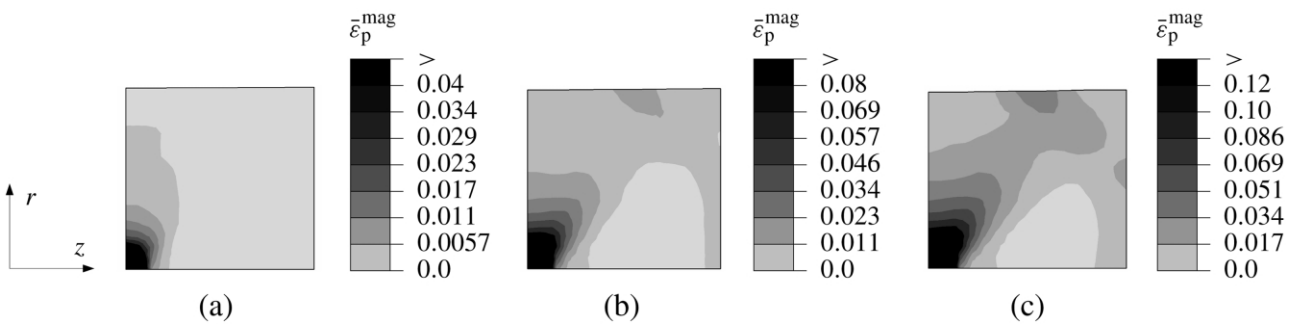

Fig. 8. Intraspherulitic magnitude of plastic deformation, $\bar{\varepsilon}_p^{mag}$, at (a) $\dot{\varepsilon}t = 0.025$, (b) $\dot{\varepsilon}t = 0.05$, and (c) $\dot{\varepsilon}t = 0.075$, for the axisymmetric SA model.

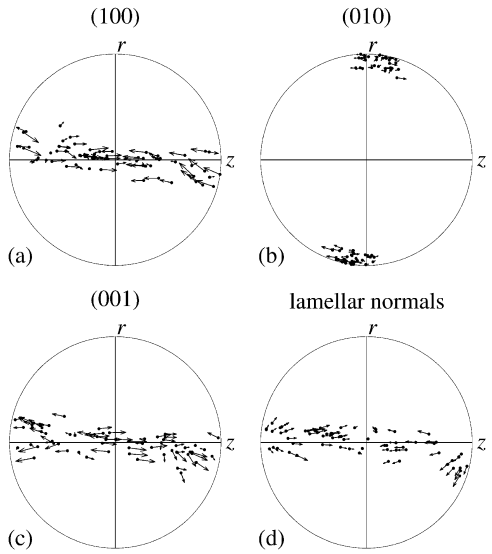

Fig. 9. Texture evolution in point A of the axisymmetric SA model, at $\dot{\varepsilon}t = 0.075$.

the convected material vector, $\mathbf{y}^{a^i} = \mathbf{F}^{a^i} \cdot \mathbf{n}_0^{l^i}$, and the current lamellar normal, $\mathbf{n}^{l^i}$. Lamellar separation is represented by $\ln(\lambda_{nn}^{a^i})$, with $\lambda_{nn}^{a^i} = \mathbf{n}^{l^i} \cdot \mathbf{y}^{a^i}$.

The (100) poles of point A, which is located in the equatorial region of the spherulite, migrate away from the tensile direction, whereas the (001) poles are moving towards the loading axis, and the (010) poles show little activity. These patterns result from deformation primarily on the (100)[001] slip system, which is the most easily activated slip system. For a small number of inclusions, also the $\{110\}\langle 1\bar{1}0\rangle$ slip systems are active. All lamellar normals are moving away from the tensile direction. The microscopic mode of deformation is found to depend on the local orientation of the lamellar normal with respect to the loading axis, as can be observed in Fig. 10. Intralamellar crystallographic deformation is found to occur predominantly for composite inclusions with their lamellar normals almost perpendicular to the tensile direction. Note that, because of the chain tilt angle, for these inclusions, the molecular chains are inclined with respect to the loading axis. Interlamellar shear is present for inclusions with their normals either inclined to or parallel to the loading direction. For the latter orientations, also interlamellar separation is observed. Negative interlamellar separation occurs if the lamellar normal direction is perpendicular to the loading direction, and is the result of conservation of volume, accompanying flow in the z-direction. In Fig. 11, a schematic overview of the occurrence of the deformation modes is depicted.

Point B is located in a region where the angle between the radial direction and the axis of loading is 45°. In this point, significant intralamellar crystallographic slip occurs only in few composite inclusions. For these domains, predominantly the (100)[010] slip system is active. Interlamellar deformation is present for those inclusions that have a relatively small angle between their lamellar normal and the loading direction (i.e. in the outer region of the pole figures). In the polar region, crystallographic slip occurs predominantly on the (100)[010] and $\{110\}\langle 1\bar{1}0\rangle$ slip systems.

The normalized equivalent mesoscopic stress, $\bar{\sigma}^{eq}/\tau_0$, and the normalized mesoscopic hydrostatic pressure, $\bar{p}/\tau_0$, are represented in Fig. 12, as well as the direction and magnitude of the normalized in-plane principal stress, $\bar{\sigma}_{max}/\tau_0$.

Deviatoric stresses are concentrated primarily in the center of the spherulite. Also in the polar region near the boundary, slightly elevated equivalent stresses are found. Large tensile triaxial stresses are observed near the

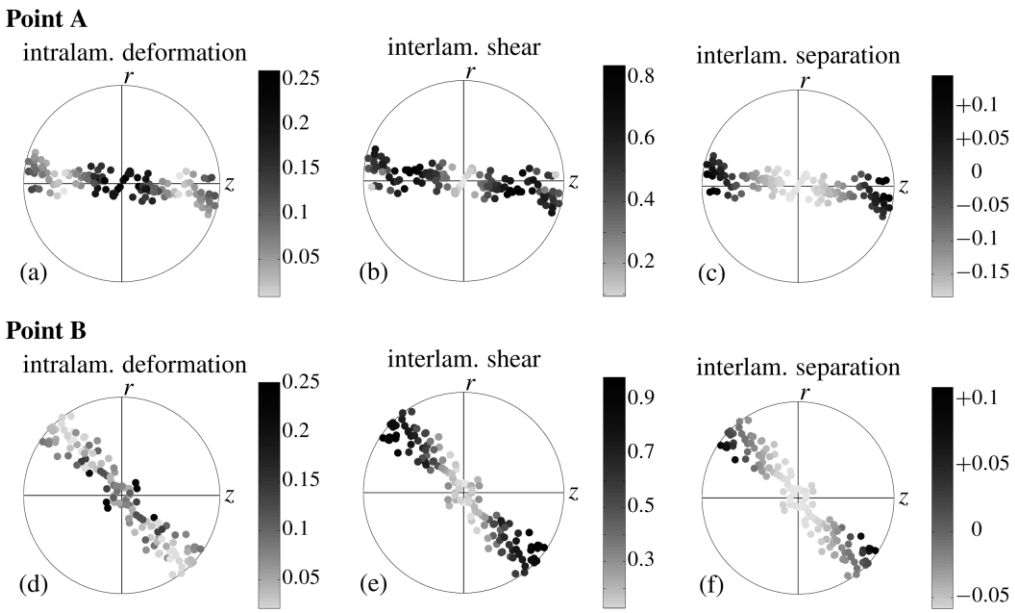

Fig. 10. Microscopic deformation results in selected points of the axisymmetric SA model, at $\dot{\varepsilon}t = 0.075$.

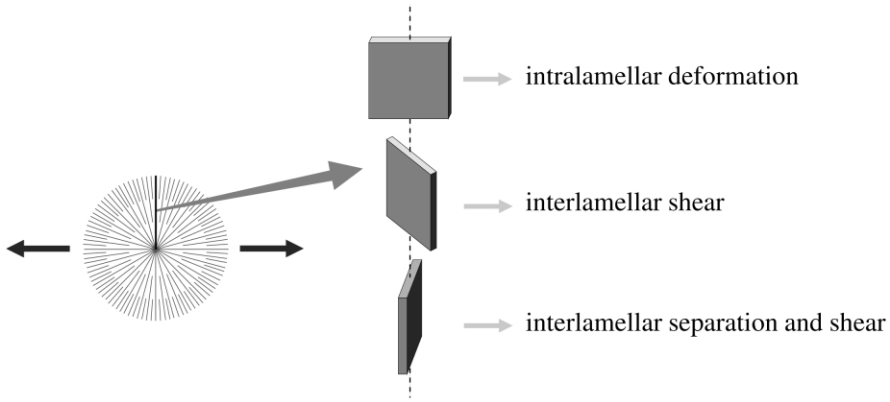

Fig. 11. Microscopic deformation modes in the equatorial region.

spherulitic boundary, and in the equatorial area, becoming larger towards the boundary. Maximum principal stresses are larger in regions of either elevated deviatoric or elevated triaxial stress, i.e. in the center of the spherulite and near the boundary, in the equatorial region. The direction of the maximum principal stress is approximately aligned with the loading direction in the entire spherulite, with a small deviation in the center and near the inclined boundary.

The dependence of the macroscopic volume-averaged axial stress, $\langle\bar{\sigma}_{zz}\rangle$, vs. the imposed deformation on the crystallinity, f^c, is represented in Fig. 13(a) for the axisymmetric SA model.

An increase of both initial stiffness and yield stress with increasing crystallinity level can be observed. In this figure, also the mesoscopic stress–strain response of a randomly oriented aggregate of composite inclusions (referred to as the *CI model*) is shown, as was used to model the response of spherulitic material in Van Dommelen et al. [32]. In the foregoing, the local mode of deformation was found to be dependent on the orientation of the crystallographic *b*-axis and on the lamellar normal orientation, i.e. on the full three-dimensional orientation of the composite inclusion. The radial coordinate within the spherulite was found to determine the amount of strain. As a consequence, the microscopic deformation mechanisms in the CI model resemble that of the macroscopic finite element model. Although the geometrical effect of the anisotropic structure within a spherulite, causing strain concentration in the center, is not present in the mesoscopic CI model, the stress–strain response observed is in reasonably good agreement with the finite element model. The influence of the crystallinity on the macroscopic yield stress is presented in Fig. 13(b). The yield stress is assumed to be given by the intersection of the initial and 5% strain tangents of the macroscopic stress–strain curve, as shown in the insert of the figure.

6.2. Plane strain

The multispherulite ID model is used to investigate the

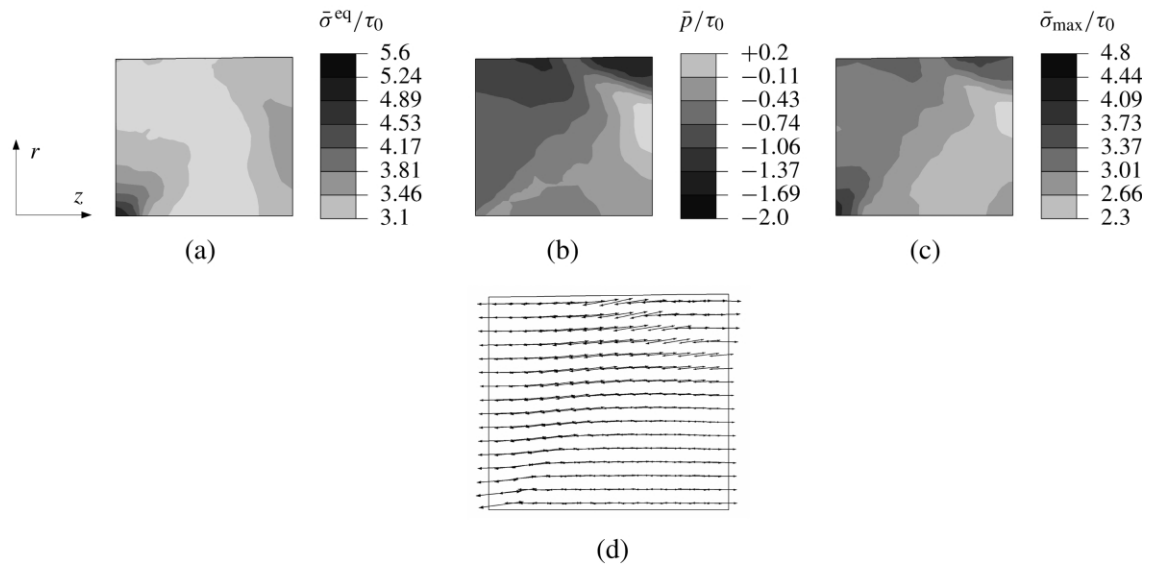

Fig. 12. (a) Normalized equivalent stress, $\bar{\sigma}^{eq}/\tau_0$, (b) normalized hydrostatic pressure, $\bar{p}/\tau_0$, and (c), (d) magnitude and direction of the normalized maximum in-plane principal stress, $\bar{\sigma}_{max}/\tau_0$, at $\dot{\varepsilon}t = 0.075$, for the axisymmetric SA model.

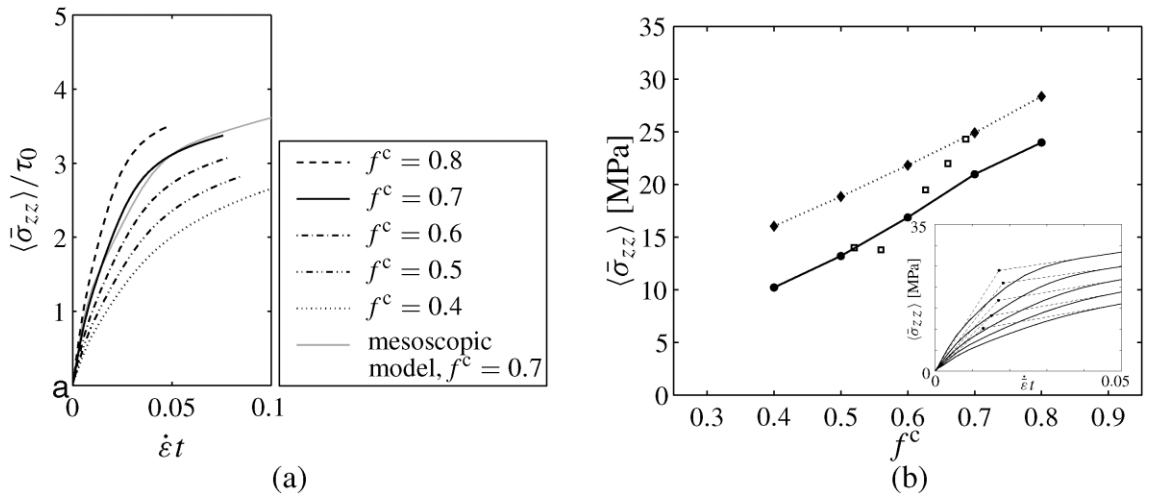

Fig. 13. The influence of the crystallinity, f^c, on (a) the normalized volume-averaged axial stress, $\langle\bar{\sigma}_{zz}\rangle/\tau_0$, vs. the imposed deformation, $\dot{\varepsilon}t$, and (b) the volume-averaged axial stress at $\dot{\varepsilon}t = 0.05$ (closed diamonds) and yield stresses (closed circles, obtained as shown in the insert), for the axisymmetric SA model. Experimental data from Ref. [59], is represented by open squares.

intra- and interspherulitic deformation of semicrystalline material under plane strain loading conditions. In Fig. 14, the obtained mesoscopic deformation and stress fields are displayed for this model.

Plastic deformation is initiated in the center of all spherulites. At larger strains, weak deformation bands appear in the inclined regions, as well as near some spherulite boundaries. Stress concentrations are observed in the centers, spreading out in the macroscopic loading direction and the free direction, and at the boundaries. In contrast to the uniaxial situation, tensile triaxial stresses are concentrated in the centers, spreading out in the inclined direction, and at some boundaries. Maximum principal stresses are found predominantly in the centers, spreading out towards the loading direction.

Additionally, more detailed results of intraspherulitic deformation under plane strain conditions are obtained with the SA model using plane strain elements and are shown in Fig. 15.

Compatibility within the staggered array of spherulites is imposed by using linear anti-symmetry conditions in the r-direction along the outer radius, replacing Eq. (8). Results compare reasonably well with the multispherulite model with an irregular stacking of spherulites, indicating that the inhomogeneous behavior is primarily governed by the anisotropic structure within the individual spherulites, and to a lesser degree from the interactions between irregularly distributed spherulites.

Some selected microscopic texture evolutions and deformation quantities are shown in Figs. 16 and 17, respectively, for the plane strain SA model.

In the area of concentrated plastic deformation, i.e. in

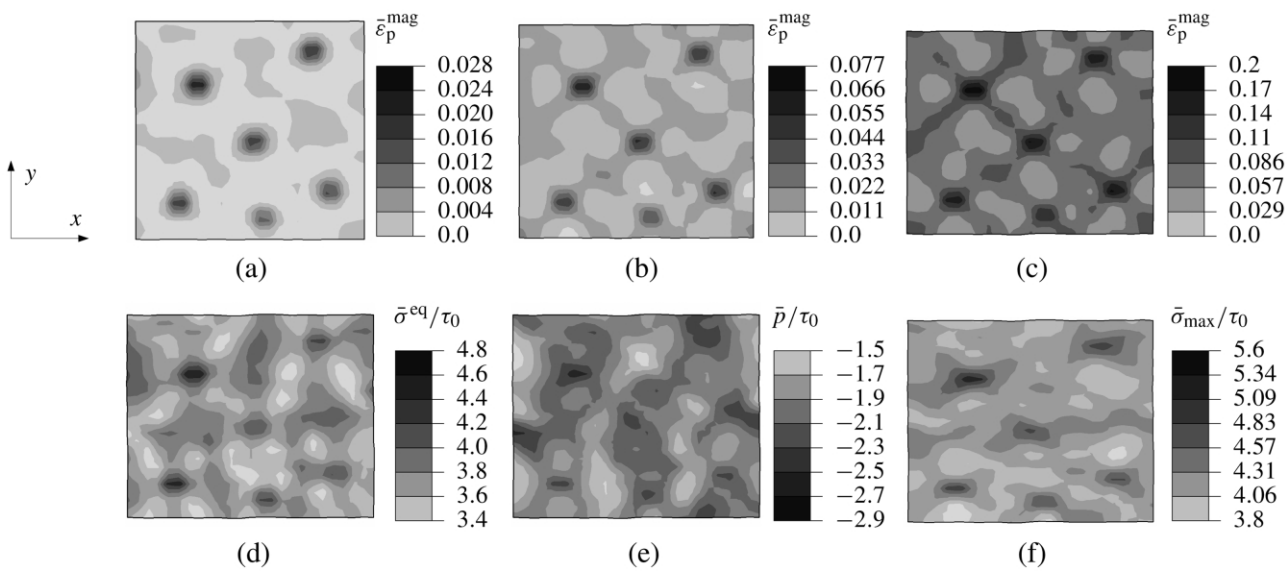

Fig. 14. Intraspherulitic plastic deformation, $\bar{\varepsilon}_p^{mag}$, at (a) $\dot{\varepsilon}t = 0.025$, (b) $\dot{\varepsilon}t = 0.05$, and (c) $\dot{\varepsilon}t = 0.1$, and (d) normalized equivalent stress, $\bar{\sigma}^{eq}/\tau_0$, (e) normalized hydrostatic pressure, $\bar{p}/\tau_0$, and (f) normalized maximum in-plane principal stress, $\bar{\sigma}_{max}/\tau_0$, at $\dot{\varepsilon}t = 0.1$, for the plane strain ID model.

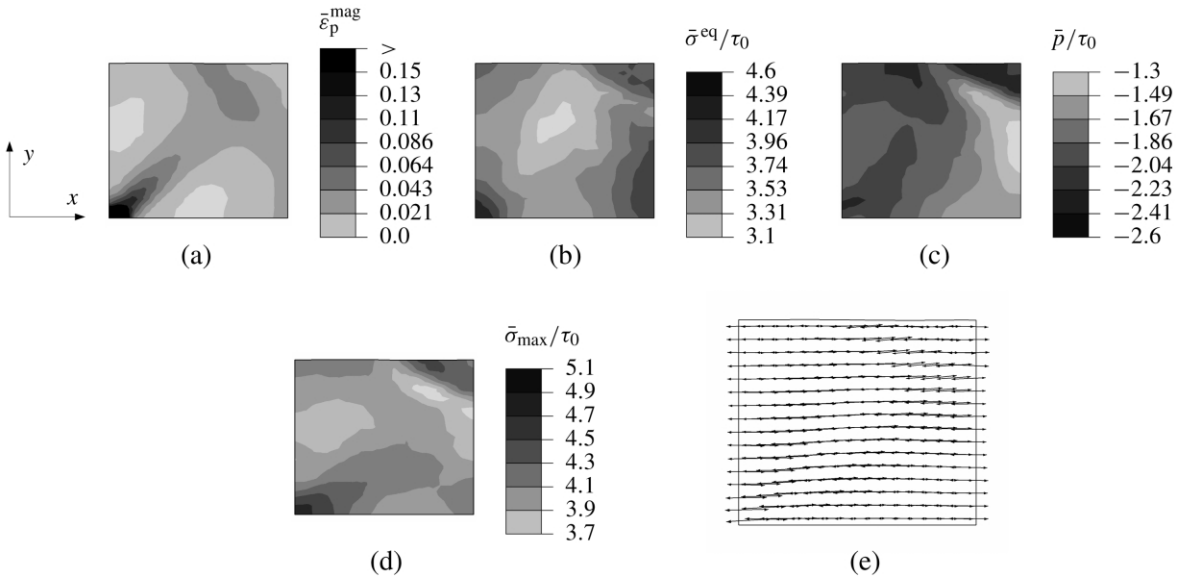

Fig. 15. (a) Plastic deformation, $\bar{\varepsilon}_p^{mag}$, (b) normalized equivalent stress, $\bar{\sigma}^{eq}/\tau_0$, (c) normalized hydrostatic pressure, $\bar{p}/\tau_0$, and (d), (e) direction and magnitude of the normalized maximum in-plane principal stress, $\bar{\sigma}_{max}/\tau_0$, at $\dot{\varepsilon}t = 0.075$, for the plane strain SA model.

the inclined direction, where point B is situated, most slip occurs on the (100)[010] transverse slip system and additionally also on the chain slip systems. Deformation in the equatorial area (point A) of the spherulite is substantially smaller than for the uniaxial loading situation. Particularly, interlamellar shear in inclusions with their lamellar normals away from the tensile direction is considerably smaller as a consequence of the plane strain condition. In this area, intralamellar deformation occurs mainly by slip on the (100)[001] chain slip system.

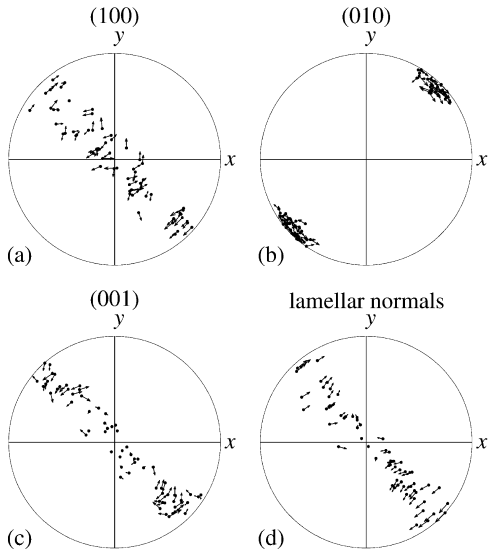

Fig. 16. Texture evolution in point B of the plane strain SA model, at $\dot{\varepsilon}t = 0.075$.

7. Conclusions

A three-level numerical model was used to study intraspherulitic deformation and stresses for semicrystalline polyethylene. The constitutive properties of the material were identified for the individual crystallographic and amorphous domains. The twisted lamellar structure of spherulitic material was represented by an aggregate of preferentially oriented two-phase composite inclusions within each material point of macroscopic finite element models of a spherulitic structure. Deformations were found to be initiated in the center, spreading out in the approximate equatorial region for uniaxial loading conditions and in inclined directions for plane strain loading. Inhomogeneous deformations were found to develop mainly as a consequence of the anisotropic structure within each spherulite, and to a lesser degree from the interactions between irregularly distributed spherulites. The deformations were linked to microstructural processes as interlamellar deformation and intralamellar crystallographic slip. Besides the dependence on the orientation of the lamellar radial direction, the local mode of deformation depends on the phase of twisting, i.e. on the interface normal orientation. Deviatoric stress concentrations were found in the center and near the polar boundary. Tensile triaxial stresses are largest near the radial boundary of the spherulite.

Acknowledgements

This research was funded by the Dutch Polymer Institute, project reference 163, ‘Deformation and fracture of polymer

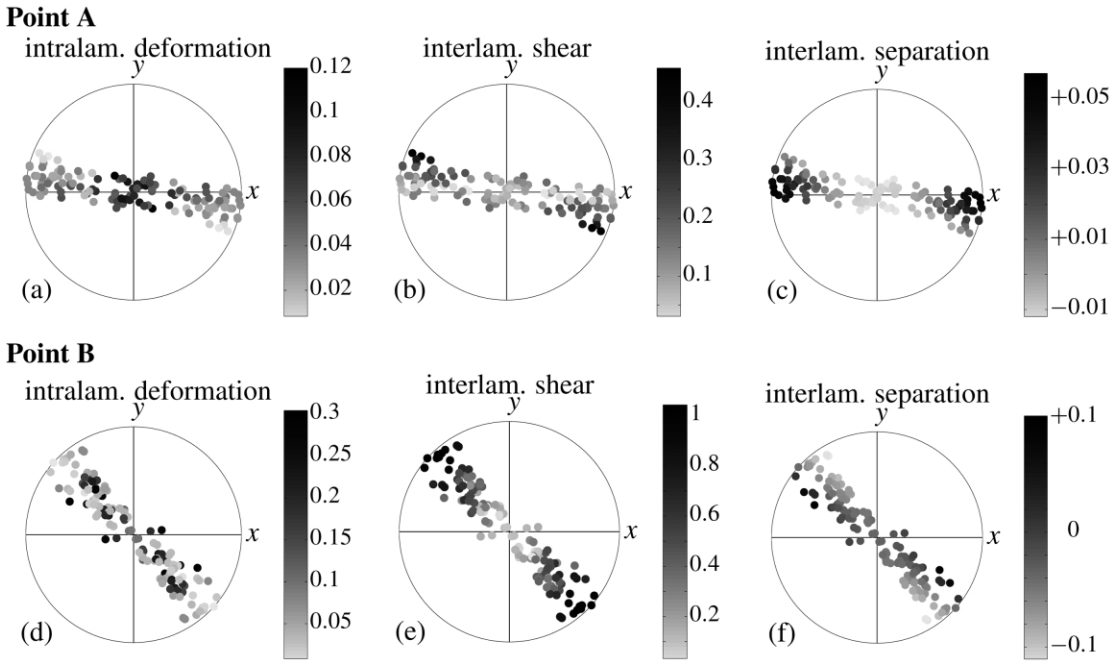

Fig. 17. Microscopic deformation results in selected points of the plane strain SA model, at $\dot{\varepsilon}t = 0.075$.

systems'. MCB and DMP acknowledge support from MIT CMSE NSF Grant No. DMR-98-08941.

References

[1] Ward IM. Structure and properties of oriented polymers. New York: Halsted Press/Wiley; 1975.
[2] Lin L, Argon AS. J Mater Sci 1994;29:294–323.
[3] G'Sell C, Dahoun A. Mater Sci Engng A 1994;175:183–99.
[4] Andrews JM, Ward IM. J Mater Sci 1970;5:411–7.
[5] Brown N, Ward IM. J Mater Sci 1983;18:1405–20.
[6] Sweeney J, Duckett RA, Ward IM. Proc R Soc Lond A 1988;420: 53–80.
[7] Parks DM, Ahzi S. J Mech Phys Solids 1990;38:701–24.
[8] Dahoun A, Canova GR, Molinari A, Philippe MJ, G'Sell C. Textures Microstruct 1991;14–18:347–54.
[9] Brooks NW, Duckett RA, Ward IM. Polymer 1992;33:1872–80.
[10] Bartczak Z, Cohen RE, Argon AS. Macromolecules 1992;25: 4692–704.
[11] Galeski A, Bartczak Z, Argon AS, Cohen RE. Macromolecules 1992; 25:5705–18.
[12] Lee BJ, Parks DM, Ahzi S. J Mech Phys Solids 1993;41:1651–87.
[13] Lee BJ, Argon AS, Parks DM, Ahzi S, Bartczak Z. Polymer 1993;34: 3555–75.
[14] Ahzi S, Lee BJ, Asaro RJ. Mater Sci Engng A 1994;189:35–44.
[15] Schoenfeld SE, Ahzi S, Asaro RJ. J Mech Phys Solids 1995;43: 415–46.
[16] Lee BJ, Ahzi S, Asaro RJ. Mech Mater 1995;20:1–8.
[17] Brooks NWJ, Duckett RA, Ward IM. J Rheol 1995;39:425–36.
[18] Argon AS. J Comput-Aided Mater Des 1997;4:75–98.
[19] Brooks NW, Unwin AP, Duckett RA, Ward IM. J Polym Sci 1997;35: 545–52.
[20] Brooks NWJ, Duckett RA, Ward IM. J Polym Sci, Part B: Polym Phys 1998;36:2177–89.
[21] Brooks NWJ, Duckett RA, Ward IM. Polymer 1999;40:7367–72.
[22] Brooks NWJ, Ghazali M, Duckett RA, Unwin AP, Ward IM. Polymer 1999;40:821–5.
[23] Bassett DC, Hodge AM. Proc R Soc Lond A 1981;377:25–37.
[24] Bassett DC, Hodge AM, Olley RH. Proc R Soc Lond A 1981;377: 39–60.
[25] Bassett DC. J Macromol Sci, Phys 2003;B42:227–56.
[26] Ward IM. Textile Res J 1961;31:650–64.
[27] Ward IM. Proc Phys Soc 1962;80:1176–88.
[28] Pinnock PR, Ward IM. Proc Phys Soc 1963;81:260–75.
[29] Stachurski ZH, Ward IM. J Macromol Sci, Phys 1969;B3:445–94.
[30] Stachurski ZH, Ward IM. J Macromol Sci, Phys 1969;B3:427–44.
[31] Owen AJ, Ward IM. J Mater Sci 1971;6:485–9.
[32] Van Dommelen JAW, Parks DM, Boyce MC, Brekelmans WAM, Baaijens FPT. J Mech Phys Solids 2003;51:519–41.
[33] Wilchinsky ZW. Polymer 1964;5:271–81.
[34] Hay IL, Keller A. Kolloid-Zeitschrift und Zeitschrift für Polymere 1965;204:43–74.
[35] Keith HD, Padden FJ. J Polym Sci 1959;41:525–8.
[36] Kobayashi K, Nagasawa T. J Polym Sci: Part C 1966;15:163–83.
[37] Wang TT. J Polym Sci: Polym Phys Ed 1974;12:145–58.
[38] Allan P, Bevis M. Phil Mag 1977;35:405–30.
[39] Allan P, Bevis M. Phil Mag A 1980;41:555–72.
[40] Butler MF, Donald AM. J Mater Sci 1997;32:3675–85.
[41] Aboulfaraj M, G'Sell C, Ulrich B, Dahoun A. Polymer 1995;36: 731–42.
[42] Brooks NW, Unwin AP, Duckett RA, Ward IM. J Macromol Sci, Phys 1995;B34:29–54.
[43] Nitta Kh. Comput Theor Polym Sci 1999;9:19–26.
[44] Doyle MJ. Polym Engng Sci 2000;40:330–5.
[45] Frank FC, Gupta VB, Ward IM. Phil Mag 1970;21:1127–45.
[46] Young RJ, Bowden PB. Phil Mag 1974;29:1061–73.
[47] Arruda EM, Boyce MC. J Mech Phys Solids 1993;41:389–412.
[48] HKS, ABAQUS/standard user's manual, version 6.2. Pawtucket, RI: Hibbitt, Karlsson & Sorensen; 2001.
[49] Van Dommelen JAW, Parks DM, Boyce MC, Brekelmans WAM, Baaijens FPT, In: Proceedings of the European Conference on Computational Mechanics, Cracow, Poland; 2001.

[50] Keller A, Sawada S. Die Makromolekulare Chemie 1964;74: 190–221.
[51] Gautam S, Balijepalli S, Rutledge GC. Macromolecules 2000;33: 9136–45.
[52] Bartczak Z, Argon AS, Cohen RE. Macromolecules 1992;25:5036–53.
[53] Socrate S, Boyce MC. J Mech Phys Solids 2000;48:233–75.
[54] Tzika PA, Boyce MC, Parks DM. J Mech Phys Solids 2000;48: 1893–930.
[55] Tvergaard V. J Mech Phys Solids 1996;44:1237–53.
[56] Tvergaard V. Int J Solids Struct 1998;30:3989–4000.
[57] Smit RJM, Brekelmans WAM, Meijer HEH. Comput Meth Appl Mech Engng 1998;155:181–92.
[58] Kamal MR, Huang T, Rey AD. J Mater Sci 1997;32:4085–99.
[59] Crist B, Fisher CJ, Howard PR. Macromolecules 1989;22: 1709–18.